nature materials

SUPPLEMENTARY INFORMATION
https://doi.org/10.1038/s41563-019-0457-6

In the format provided by the authors and unedited.

Synthetic spin–orbit interaction for Majorana devices

M. M. Desjardins[1,4], L. C. Contamin[1,4], M. R. Delbecq[1], M. C. Dartiailh[1], L. E. Bruhat[1], T. Cubaynes[1], J. J. Viennot[2], F. Mallet[1], S. Rohart[3], A. Thiaville[3], A. Cottet[1] and T. Kontos[1*]

[1]Laboratoire de Physique de l'Ecole Normale Supérieure, ENS, Université PSL, CNRS, Sorbonne Université, Université Paris Diderot, Sorbonne Paris Cité, Paris, France. [2]Univ. Grenoble Alpes, CNRS, Grenoble INP, Institut Néel, CNRS, Grenoble, France. [3]Laboratoire de Physique des Solides, Université Paris-Saclay, CNRS UMR 8502, Orsay, France. [4]These authors contributed equally: M. M. Desjardins, L. C. Contamin. *e-mail: kontos@lpa.ens.fr

Supplementary Information

"Synthetic spin orbit interaction for Majorana devices"

M.M. Desjardins[1,†], L.C. Contamin[1,†], M.R. Delbecq[1], M.C Dartiailh[1], L.E. Bruhat[1], T. Cubaynes[1], J.J. Viennot[2], F. Mallet[1], S. Rohart[3], A. Thiaville[3], A. Cottet[1] and T. Kontos[1]*

[1] Laboratoire de Physique de l'Ecole Normale Supérieure, ENS, Université PSL, CNRS, Sorbonne Université, Université Paris Diderot, Sorbonne Paris Cité, Paris, France

[2] Institut Néel, CNRS, 25 rue des Martyrs, 38042 Grenoble cedex 9, France

[3] Laboratoire de Physique des Solides, Université Paris-Sud et CNRS, Bât. 510, 91405 Orsay Cedex, France

*To whom correspondence should be addressed: kontos@lpa.ens.fr

This Supplementary Information is organized as follows.

1. Modelling of the probe and dressed nanotube density of states and fit of the conductance
    a. Usadel equations used to characterize the superconducting contacts
    b. Effect of a S' type probe
2. Additional data on the main device (with the magnetic texture):
    a. Large scale device layout,
    b. Gate dependence of SGSs,
    c. Additional conductance maps,
    d. Control experiments on the zero-bias peak.
3. Additional data on control devices (without the magnetic texture).
4. Magnetic characterization of the Co/Pt multilayer.
5. Estimation of the synthetic spin-orbit energy from the SGSs oscillations
6. Analytical theory of the oscillations of Subgap states with magnetic field
7. Numerical study of the synthetic spin-orbit: oscillations of subgap states and emergence of Majorana zero energy modes:
    a. Illustrations of the different scenarios of figure 3c
    b. Implementation of a realistic model for the stray fields (from the MFM data shown in figure 1e and micro-magnetic simulations) showing the robustness of our observations with respect to a disordered magnetic texture.
    c. Simulation of Majorana bound states in our geometry with a magnetic texture and superconductivity induced from the side of the wire. This simulation shows similar features to the observed zero-bias peak.

1. Modelling of the probe and dressed nanotube density of states and fit of the conductance

This section describes the modeling of the superconducting contacts introduced in Fig. 1. The fit is described in details, and Figure S2d shows its good agreement with the experiment. We also comment on the effect of a S' probe, and notably the fact that the differential conductance does not directly corresponds to the density of states.

a. Usadel equations used to model the superconducting contacts

We present in this section the theory which allows us to account well for the shape of the full conductance curves based on the quasiclassical theory of superconductivity in the diffusive regime (Usadel equations). We use a superconducting bilayer of Nb(40nm)/Pd(4nm) to make a superconducting contact on the nanotube. The density of states in these bilayers are in general non BCS because of interface resistance between the superconducting slab and the normal slab and inverse proximity effect. In addition, in our case, the dipolar cycloidal-like field can induce a pair-breaking which can be taken into account via an Abrikosov-Gorkov general term. The Usadel equations gives the evolution of the pairing amplitude in the Pd layer with the distance to the superconductor's interface, z. It reads:

$$\frac{\hbar D}{2}\partial_z^2\vartheta(z) - (-iE+\gamma)sin\vartheta(z) - 2\Gamma_{AG}sin\vartheta(z)cos\vartheta(z) + \Delta(z)cos\vartheta(z) = 0$$

where E is the energy, D is the diffusion constant, $\Gamma_{AG}$is the Abrikosov-Gorkov pair-breaking parameter, γ is the "Dynes" parameter and $\Delta(z)$ is the gap function. The pairing angle $\vartheta(z)$ is related to the normal and anomalous Green's functions in the Pd contact, G and F respectively, via the relation: $G(z) = cos\vartheta(z)$ and $F(z) = sin\vartheta(z)$. The density of states is $N(z, E) = Re(cos\vartheta(z))$.

An important energy scale controlling the physics of proximity effect in the bilayer is the Thouless energy $E_{Th} = \frac{\hbar D}{d^2}$, where d is the thickness of the normal (Pd) slab. In our case, this energy is much larger than the superconducting gap Δ of the homogeneous superconductor, and the interface is not too opaque (as shown by the large induced gap). Neglecting the self-consistency of the superconducting gap, one may approximate the pairing angle by the homogeneous solution which obeys the following implicit equation:

$$tan\vartheta_0 = \frac{\Delta}{-iE + \gamma + 2\Gamma_{AG} cos\vartheta_0}$$

The above equation may be solved numerically and the gap appearing in it has the meaning of an effective gap in the normal slab. The normalized density of states in each of the Pd buffer contacting our nanotube is therefore $N(\Delta, \gamma, \Gamma_{AG}, E) = Re(cos\vartheta_0)$.

In order to compute the current I flowing through our device and the corresponding conductance $G = dI/dV_{sd}$, one may use the above density of states. As explained in the main text, one of the two contact is a tunnel probe and the nanotube is only in good contact with the other. One can therefore approximate the density of states of the latter by that of the Nb/Pd bilayer which induces the superconducting correlation in it and a sum of two lorentzians describing the subgap states:

$$N_{NT}(E) \approx N(\Delta, \gamma, \Gamma_{AG}, E) + \beta \sum_{i=+/-} \frac{\eta}{(E - i \times E_{SGS})^2 + (\eta/2)^2}$$

This equation is an approximation since it neglects the transfer of spectral weight from the density of states of the slab to the subgap states and is only valid as long as $\frac{4\beta}{\eta} < 1$. The tunnel current can be expressed using the usual tunnel spectroscopy formula:

$$I = \frac{G_N}{e} \int_{-\infty}^{+\infty} dE\, N_{NT}(E) N\big(\Delta, \gamma_2, \Gamma_{AG,2}, E + eV_{sd}\big)[f(E) - f(E + eV_{sd})]$$

where $f(E)$ is the Fermi function and G_N is the normal state conductance. Deriving with respect to V_{sd}, we obtain the conductance

$$G = G_N \int_{-\infty}^{+\infty} dE\, N_{NT}(E) N\big(\Delta, \gamma_2, \Gamma_{AG,2}, E + eV_{sd}\big) \left(-\frac{\partial f}{\partial E}\right)_{E+eV_{sd}}$$

$$+ G_N \int_{-\infty}^{+\infty} dE \frac{\partial N}{\partial E}\big(\Delta, \gamma_2, \Gamma_{AG,2} E + eV_{sd}\big) N_{NT}(E)[f(E) - f(E + eV_{sd})]$$

The above formula is the one used to fit the cut in Fig. 1c to extract the DOS shown in Fig. 1d. We allow the Abrikosov-Gorkov Γ_{AG} and the Dynes parameter γ to be different for the left and the right tunnel contact.

The fit presented in Fig 1d and in more details in Supplementary Fig. 2d was obtained with $E_{SGS} = 210\ \mu eV$, $\eta = 79\ \mu eV, \Delta = 716\ \mu eV$, $\Gamma_{AG} = 51\ \mu eV$, $\Gamma_{AG,2} = 318\ \mu eV$, $\gamma_1 = 16 \mu eV$, $\gamma_2 = 82\ \mu eV, \frac{4\beta}{\eta} = 0.74$, T=150mK and $G_N = 0.61\ \frac{e^2}{h}$. This leads to two density of states N_{NT} (contact 1) and N (contact 2), plotted in Fig. 1d.

<u>b. Effect of a S' type probe</u>

From the fit, contact 2 has a large residual density of states at the Fermi energy (which we call later on a S' contact). Since its density of states N is non constant in energy, the second term in the above conductance equation is non-zero.

As a consequence, the heigth of the SGSs conductance peaks is not directly linked to their spectral weight (as it would for a normal tunnel probe). This effect explains why the oscillations of the SGS energies leads to the variation of the SGSs conductance height seen in Fig. 2b.

Importantly, this also shows that the very low value of conductance associated to the two Subgap states does not imply low spectral weights in $N_{NT}(E_{SGS})$. This is best seen on Fig. 1d where the peak height of the two Subgap peaks amounts to about 0.74 of the normal state density in the nanotube. Similarly, the zero bias peak has a spectral weight much larger than its height in conductance. From the comparison with the height of the Subgap states which are roughly twice as large, we can estimate that the actual peak height of the zero bias peak is about 0.35 of the normal state density of states in the nanotube.

This fit finally shows that we can safely remove that background from the bare curves shown in Supplementary Fig. 3 to plot those of Fig. 4c in the main text.

2. Additional data on the main device (with the magnetic texture):

We present in this section several additional measurements on the magnetic texture device. We first in figure S1 give a larger image of the device, where the gates G and G' are visible as well as the RF input lines used for Fig. S5. Figure S2 shows the evolution of conductance as a function of gate G', not used in the main text, for two values of gate G. It shows Fabry-Pérot-like patterns, from which we extract the level spacing δ. Figure S3 shows the conductance map of figure 4a without removing the background conductance signal, showing that the both the ZBP and the SGSs peaks are still clearly visible. Figure S4 shows the conductance map at larger values of the magnetic field, where the closing of the superconducting gap is visible. Figure S5 and S6 present control experiments, where the conductance is studied as a function of a RF tone and temperature. Figure S7 present additional data on the hysteretic behavior at low magnetic field. It shows that the hysteresis is present only when the ZBP is present. Figure S8 present the evolution of conductance as a function of gate G over a larger bias window, showing that the coherence peak do not move.

a. Large scale device layout and microwave environment. The large scale device layout and microwave environment is shown in Supplementary Fig. 1. The whole device is embedded into a microwave cavity which has a fundamental resonance frequency of about 7.5 GHz. For the device presented in the main text, this particular mode was not coupled to the device but other modes of the electromagnetic environment were coupled. We use here these modes to couple our device with a distant gate Gate G (with gate voltage V_g) which is the one used in the main text. The device is also coupled via the bottom gate to Gate G' with gate voltage $V_{g'}$.

These two gates have different effects on the device. Gate G' has a larger capacitance to the bottom gate than Gate G, thus sets mainly the potential of the bottom gate. The effect of Vg' is to tune the energy levels in the NT, as shown by figure S2. Vg affects neither the subgap states, nor the gap and only controls the appearance of the ZBP in the conductance, which goes along with an increase of the conductance background. This could be linked to a more specific effect of gate G that would locally change the wavefunction in the NT, finely tuning the overlap of the ZPB wavefunction to the contact electrodes.

Although the specific resonant mode of the cavity was not coupled to our device, the coplanar waveguide resonator could be used to convey a microwave signal in the GHz range to study its dynamical response (see below).

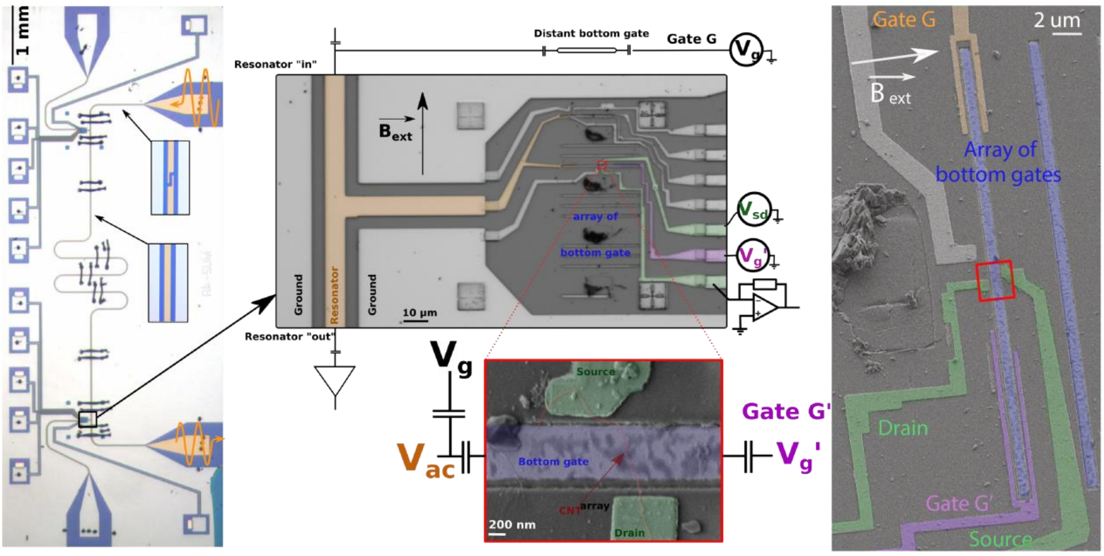

Supplementary Figure 1 | Microwave environment of the device. The whole device is embedded in a microwave cavity with a resonance frequency of about 7.5 GHz.

Gate map of subgap states. We present the gate map of the Subgap states when Gate G is kept at 0V and Gate G' (which is directly coupled to the bottom gate as shown in Supplementary Fig. 1) is swept from 0.2V to 1V in Supplementary Fig. 2. The Subgap states remain visible essentially in all the map. A parity crossing is observed at $V_{g'}$~0.7V. Importantly, the high bias conductance, close to e^2/h displays only weak features. In particular, no Coulomb blockade diamond is observed which signals that our experiment is in the Fabry-Pérot regime. From the smooth chessboard pattern, one can extract an estimate of the level spacing δ ~1.5 meV.

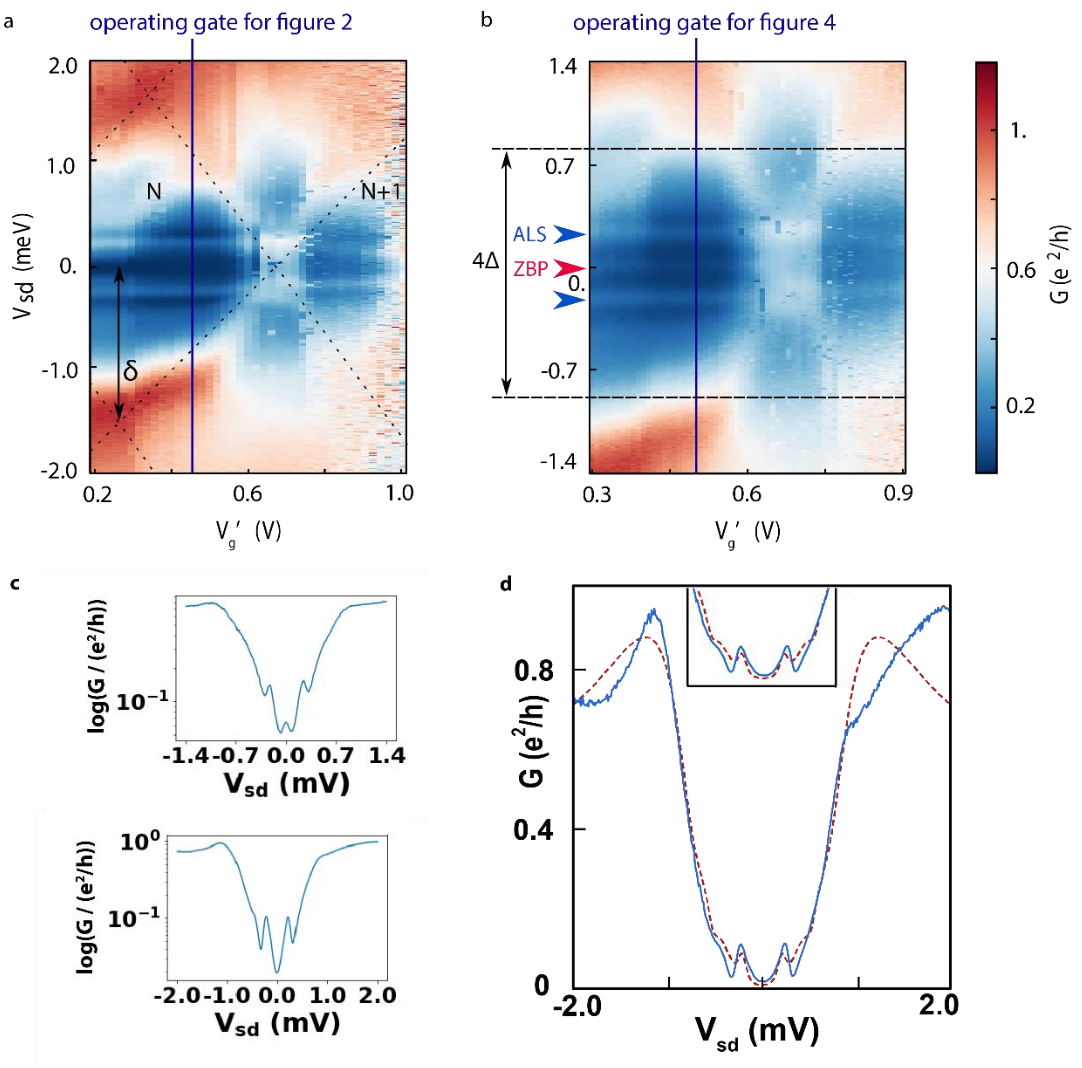

Supplementary Figure 2 | Gate map of the Subgap states. a,b. Conductance as a function of bias V_{sd} and Gate G' ($V_{g'}$) showing the evolution of the Subgap states as a function of $V_{g'}$ for two values of Gate G, V_g=0V (panel a) and -3V (panel b) such that the Zero Bias Peak is present. In panel a, the shape of the Fabry-Pérot modulations of the conductance is highlighted by the dotted black lines, and N and N+1 indicates the equilibrium charge on the dot. The level spacing δ for our quantum dot can be roughly estimated, as shown by the black arrow. In panel b, the edge of the superconducting gap and the position of the different peaks studied are outlined. The values of Gate G' for the different figures of the article are shown by the blue lines. **c.** Corresponding superconducting gap in log scale, at $V_g = 0V$ (bottom) and -3V (top). **d.** Comparison between the conductance measurement as a function of bias (blue line) and the corresponding fit using the Usadel equations (red dashes).

c. Conductance maps with background and gap closure at high magnetic field. We present in this section two conductance maps corresponding to those of the main text. In Supplementary Fig. 3, we present the raw data corresponding to Fig. 4a. In this map, one can see that there is a strong depression of the conductance as a consequence of the superconducting gap. After fitting the above curves with the theory presented above, one can extract the contribution arising only from the Subgap states which allows one to observe more clearly the magnetic field dependence of these states. Nevertheless, as one can see in Supplementary Fig. 3, all the features presented in the main text are visible in the raw data.

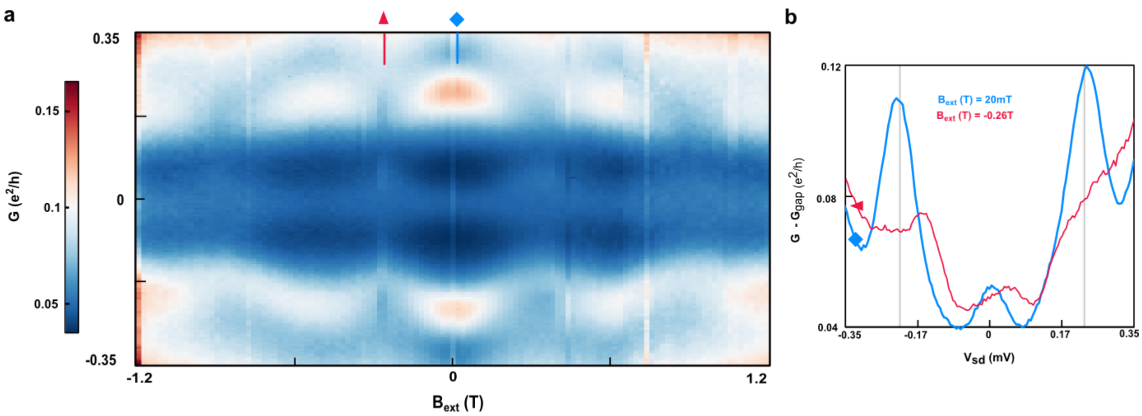

Supplementary Figure 3 | Conductance map with background. Raw data of the conductance as a function of bias V_{sd} and the external magnetic field B_{ext} at $V_g = -3V$. As shown in the map and the cuts corresponding to those of the main text, the Subgap resonances as well as the zero bias peak are clearly visible also in the raw data. The background originates from the peculiar shape of the density of states in the proximized Pd/Nb bilayer.

Finally, it is interesting to study the magnetic field map of the conductance up to large fields where the superconducting gap of the electrodes starts to weaken substantially. In Supplementary Fig. 4, we present such a map where the magnetic field is swept from 0T to 2T and back to 0T. As expected, we observe a gradual "square root like" decrease of the gap edge (the coherence peaks are not visible in this bias window).

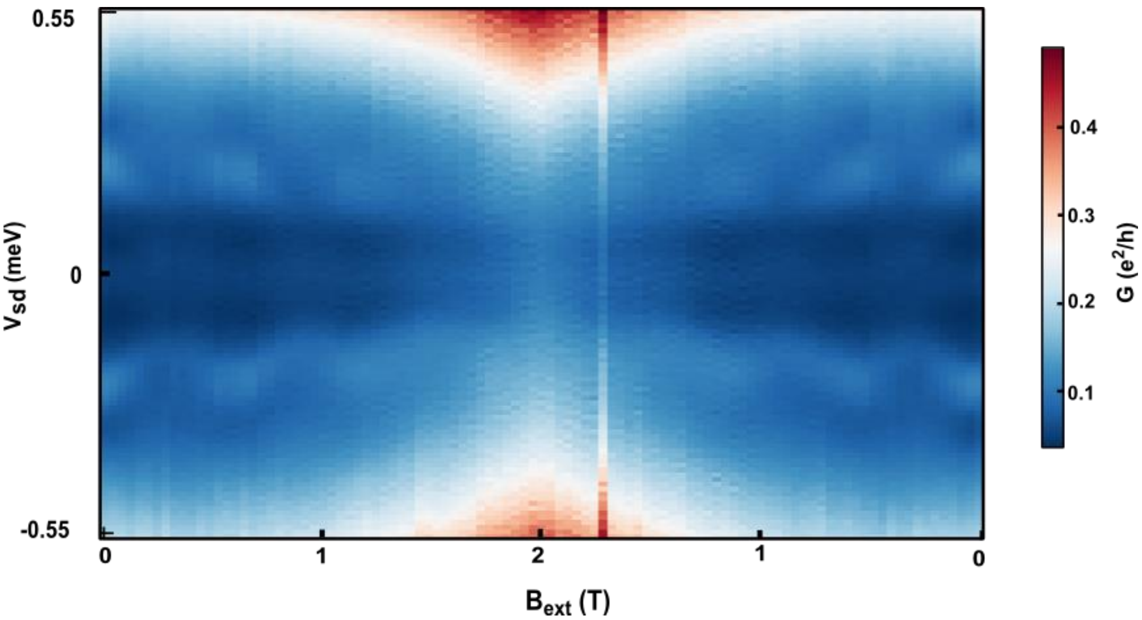

Supplementary Figure 4 | Gap closure at high magnetic field. Conductance map in the V_{sd}-B_{ext} plane from 0T to 2T and back showing the gradual decrease of the superconducting gap. The map is taken at V_g=3V.

d. Control experiments: Microwave power and temperature dependence of Subgap states and zero bias peak. In this section, we present two control experiments. In the first, we apply a large microwave power to the input port of the microwave cavity in order to test whether the zero bias peak may arise from a weak Josephson effect. In the adiabatic limit where the frequency of the applied tone to the cavity $f_{rf} = 5{,}6$ GHz is much smaller than the relevant relaxation rates of the states in the device, the conductance G is modulated by the cavity photons as:

$$G(t) = G\big(V_{sd} + V_{AC}\cos(2\pi f_{rf} t)\big)$$

The conductance can be fit by 3 lorentzians centered around each of the peak energies as shown in the section devoted to the finite bias conductance. The phenomenology of the above equation is simply a splitting of each conductance peaks if V_{AC} bias larger than their width. As shown in Supplementary Fig. 5, the two finite energy Subgap states as well as the central peak split at the same power and in the same way showing that they all correspond to electronic states characterized by a lorentzian like spectral density. In particular, these measurements are not consistent with the zero bias peak being a well-developed Josephson supercurrent branch which would display Shapiro steps. The case of a weak Josephson branch which does not display Shapiro steps would be very quickly washed out by temperature (at the temperature scale given by the Josephson energy, ie a supercurrent of 1nA corresponds to 140mK) and is not consistent with the temperature dependence of the zero bias peak which is described below.

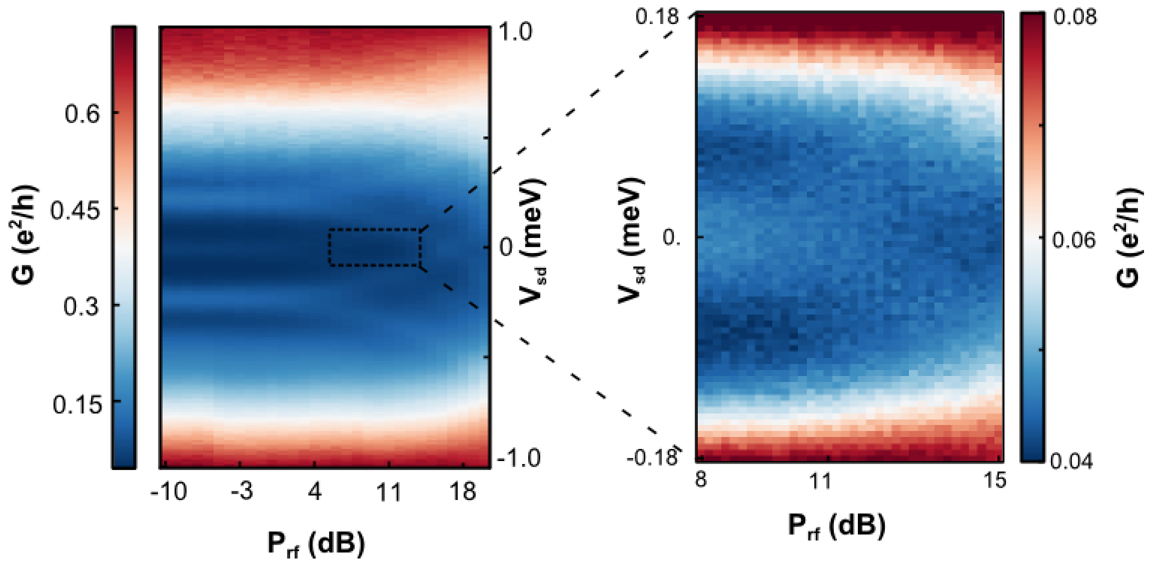

Supplementary Figure 5 | Microwave power dependence of Subgap states and zero bias peak. Evolution of the Subgap peaks as a function of the microwave power applied at the input of the cavity.

Finally, we present in Supplementary Fig. 6 the temperature dependence of our measurements which is fully consistent with a gradual filling of the gap which starts to be effective only at about 1K. In particular, as one can see in panel a of Supplementary Fig. 6, we observe that the zero bias peak and the Subgap states disappear at the same temperature (about 1K). Therefore, we can exclude a thermal occupation origin for the zero bias peak that would be indicated by a continuous increase of the zero bias peak as a function of temperature.

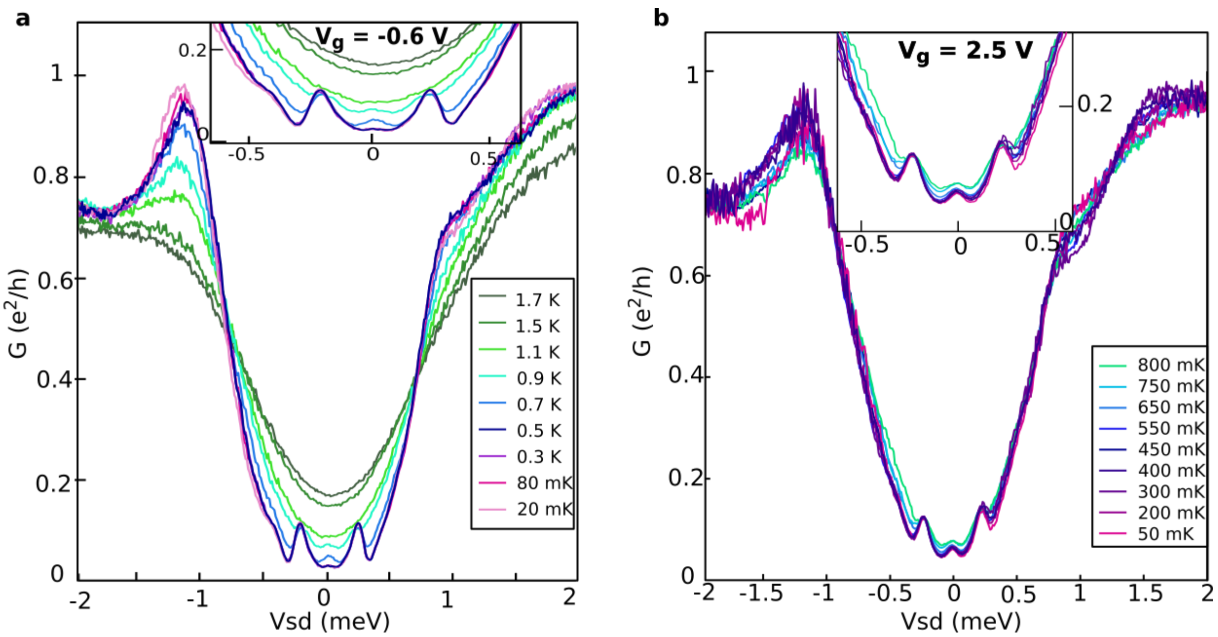

Supplementary Figure 6 | Temperature dependence of Subgap states and zero bias peak. **a.** Evolution of the Subgap peaks as a function of the temperature from 20 mK to 1.7K for Vg=-0.6V. We interpret the higher peak for T=700mK as a small gate switch because the gate setting is close to the transition at which the zero bias peak emerges. Such a switch is absent in panel b which is for a gate setting further into the gate region where the zero bias peak appears. **b.** Evolution of the Subgap peaks as a function of the temperature from 50 mK to 800mK for Vg=2.5V.

Magneto-resistance and hysteresis at different gate voltages V_g. Supplementary Fig. 7 displays a panel of the conductance maps $V_{sd} - \mathrm{B_{ext}}$ for different gate voltages between 0 and -3V. We observe that the SGSs are insensitive to small magnetic fields, whereas the zero bias peak and the background shows a magneto-resistance provided the zero bias peak is present. These two different behaviours are also observed in the Gate G dependence that leaves the SGSs unchanged. However we cannot match this magnetoresistance with a shift in gate voltage. We also present the emergence of the hysteresis of the zero bias peak with the gate voltage which is directly linked to the emergence of the peak.

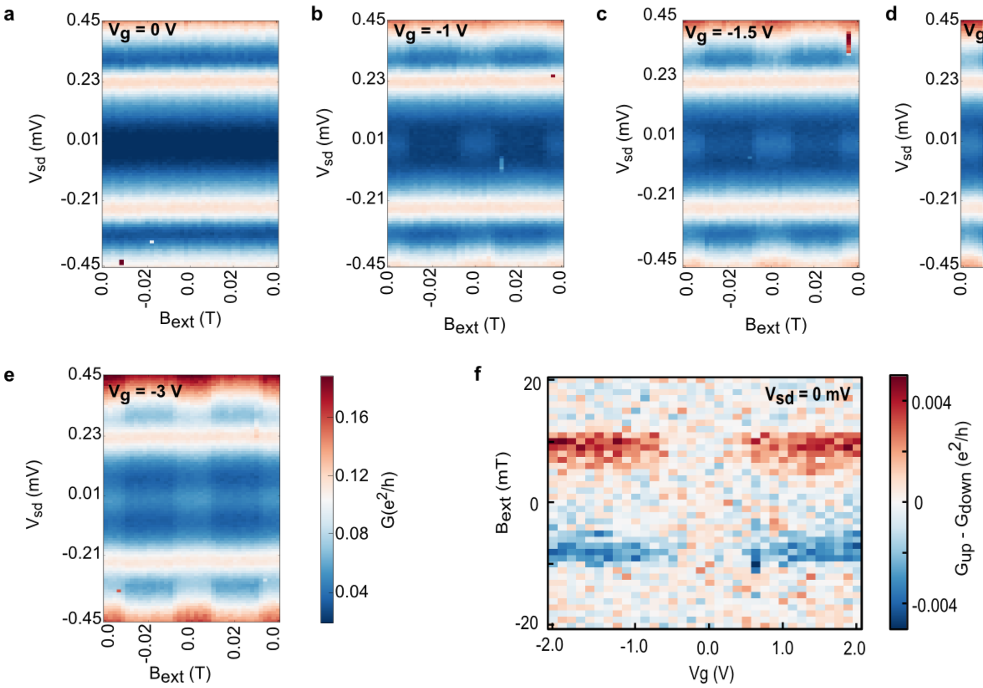

Supplementary Figure 7 | Hysteresis of the zero bias peak. a-e. Conductance map $\mathrm{B_{ext}}$-$\mathrm{V_{sd}}$ at small magnetic field for different gate voltages. The presence of the vertical stripe corresponding to the magnetoresistance is correlated to the emergence of the zero bias peak. **f.** Difference in conductance between upward and downward field sweeps at zero bias showing the gate voltage dependence of the hysteresis.

Evolution of the conductance as a function of V_g over a large V_{sd} range Supplementary Fig. 8 displays a panel of the conductance maps $V_{sd} - \mathrm{V_g}$ with no magnetic field applied. We observe that the coherence peaks do not move although the background conductance slightly changes. As a comparison, two conductance cuts are shown at B=0T and B=600mT, where the start of the closing of the superconducting gap is visible.

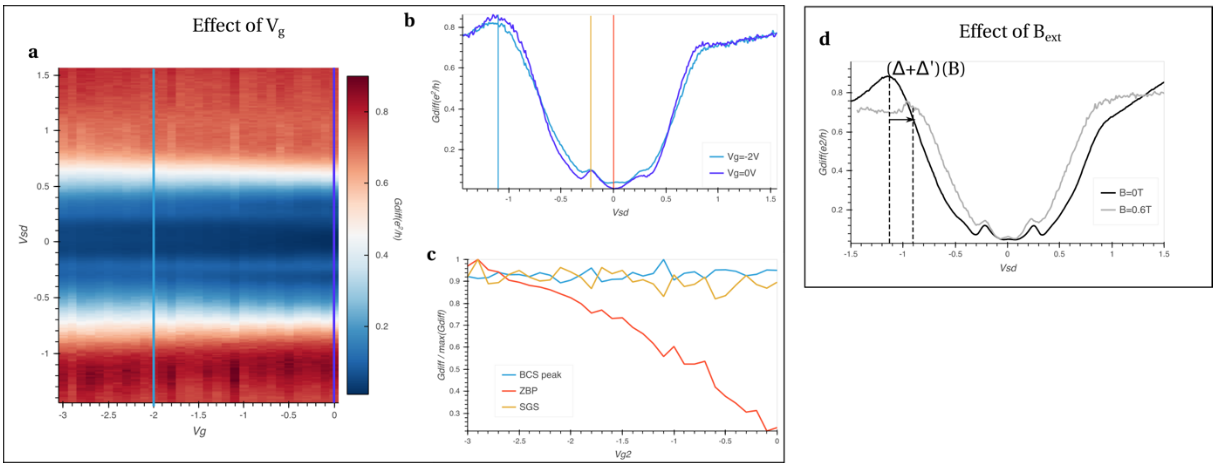

Supplementary Figure 8 | $V_{sd} - \mathrm{V_g}$ maps with a large bias window. a. Conductance map $V_{sd} - \mathrm{V_g}$. **b.** Two cuts at positions represented by the blue lines in panel a. **c.** Evolution of the conductance at different bias voltages, corresponding to the ZBP, the SGS peak at V_{sd}<0 and the coherence peak, as represented by the colored lines in panel b. We see that only the ZBP conductance increases when the gate voltage decreases. **d.** Evolution of the conductance over the same bias window for two values of B_{ext}, 0 and 600mT. We see a clear evolution of the coherence peak position.

3. Additional data on the control devices.

In this section we describe conductance measurements as a function of gate voltage, bias and magnetic field for three supplementary S/QD/S devices with no Co/Pt magnetic texture.

Of these three devices, two clearly display Coulomb blockade diamonds of a S/QD/N-like system, and one present a superconducting gap with Andreev Bound States visible between $eV_{sd} = \Delta$ and 2Δ. These measurements illustrate that in our experiment we systematically observe a S/QD/S' behaviour, where one probe has a residual density of states at the Fermi *energy. We do not observe oscillations of SGSs as a function of magnetic field in these devices. In this section, we also give the details of the equations yielding the fit for the conductance data as a function of B_{ext} of the control device shown in Fig. 3.*

Supplementary Fig. 9 and 10 show additional characterizations of the control device presented in Fig. 3 of the main text, as well as transport measurements on two additional control devices. These devices consist in S/QD/S circuits with no Co/Pt magnetic texture, and were fabricated in order to understand further the specificity of our observations.

Supplementary Fig. 9 shows the $V_g - V_{sd}$ conductance map for three different devices at two values of magnetic field, while Supplementary Fig. 10 shows the evolution of these transport peaks as a function of an in-plane external magnetic field B for devices a and b.

We observe two regimes: either ABS are visible, in device *A*, or only peaks corresponding to quasiparticle transport in devices *B* and *C*.

First, the conductance of device *A* is illustrative of transport through ABS below the superconducting gap, between $eV_{sd} = \Delta$ and 2Δ. In Supplementary Fig. 10(a-c) we show that in this device, away from the charge degeneracy points, the subgap states are fixed at $eV_{sd} = \Delta$. Looking at their evolution in magnetic field, we only observe the closing of the superconducting gap. Indeed, in this device we have a zero or weak constant spin-orbit interaction. From the scenarii A and B of section 6a, ABS should display crossing oscillations with a period $\tilde{B}_{ext}$ of the order of $\delta/g\mu_B$ = 5T for our parameters, which explains why they stay pinned to the superconducting gap until it closes. We observe two square-root-like decrease of the gap for both a peak at $eV_{sd} = \Delta$ and $eV_{sd} = 2\Delta$, expected for a S/QD/S' device with a S' contact with a residual density of states at the Fermi energy. At higher bias, we observe Coulomb diamond, indicating an important charging energy in the system.

Secondly, in the devices presented in Supplementary Fig. 9b and c (devices *B* and *C*), we observe clear Coulomb diamonds, shifted by an energy gap Δ. Although the two contact electrodes are made of superconductors, the conductance maps can be interpreted as transport signatures through a S/QD/N system (see e.g. ref[36]), with the superconducting gap of the S electrode shifting the Coulomb diamonds, as in the case with a magnetic texture device. This shows that one of the S contact has often a large depairing parameter which yields a smoothly varying density of states dubbed S' (mimicking a N contact with a reduced density of states around the Fermi energy). There is also a residual density of states in the superconducting contact S, which gives rise to a weak quasiparticle peak below the superconducting gap.

Device *B* is the control device presented in figure 3 of the main text. The control device displays clear Coulomb diamonds as shown in Supplementary Fig. S9b, at 0T and 1.7T.

Supplementary Fig. S10 e show the evolution of the transport peaks in magnetic field, from which the peaks positions of Fig. 3b are extracted. We observe the closing of the superconducting gap with B. Contrarily to subgap states, the quasiparticle resonance simply splits linearly.

The superconducting critical field for the control device *B* is lower than the one of the magnetic texture device due to the change in the Nb electrode thickness (150nm instead of 40nm).

We use a constant interaction model to obtain the stability diagram equations for a S/QD/N system, used in the fit of Fig. 3b (blue and red dashed lines). The quasiparticle peaks positions is given by $eV_{sd} = \frac{\epsilon(B)}{\alpha}$ and $eV_{sd} = -\frac{\epsilon(B)}{1-\alpha}$, where α is the contact asymmetry and $\epsilon(B) = (\epsilon_0 - \frac{1}{2} g \mu_B B)$ is the chemical potential of the dot (for a spin down electron, in agreement with the diamond shifting to the left with magnetic field as seen in Supplementary Fig. 9b).

The superconducting gap coherence peaks positions are given by $eV_{sd} = (\Delta(B) - \epsilon(B))/(1-\alpha_2)$ (at positive bias) and $eV_{sd} = -\frac{\Delta(B)+\epsilon(B)}{1-\alpha}$ (at negative bias) where $\Delta(B) = \Delta\sqrt{1-\left(\frac{B}{B_c}\right)^2}$. Here we used different contact asymmetries between positive (α_2) and negative (α) bias to fit the data, as one can see in Supplementary Fig. 9b that the slope does change.

One can note that since the diamonds shifts in energy, the lower gap evolution should be piecewise-defined. However the critical field is reached before this is needed.

The fit values are the following: Δ = 0.68 meV; B_c = 0.6 T; ϵ_0 = -0.02 meV; g = 3.8; α= 0.31; α_2 = 0.47.

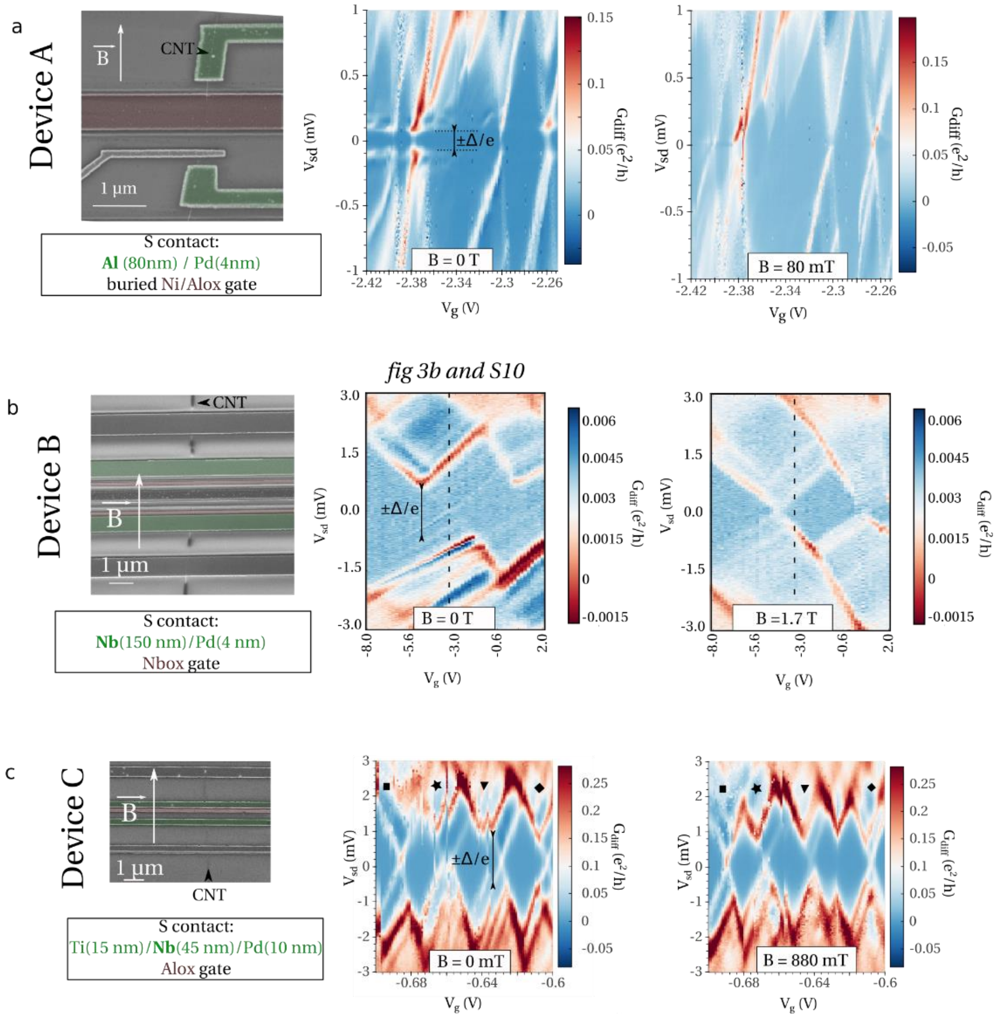

Supplementary Figure 9 | Characterization of the control devices. The three control devices are S/QD/S' circuits). The superconducting contacts are represented in green, the gate Vg in brown. **a.** Control device *A*. False-color SEM image and V_g-V_{sd} conductance map for an Al/QD/Al device with a bottom Ni/AlOx gate, made with the stamping technique, at 0 and 80 mT (where the Al gap closes **b.** Control device *B*. False-color SEM image and V_g-V_{sd} conductance map for a Nb/QD/Nb device with a bottom NbOx gate, at 0 and 1.7 T (corresponding to the closing of the Nb gap). The dashed line indicates a reference gate voltage, to illustrate the shift in the Coulomb peaks due to Zeeman effect. **c.** Control device *C*. False-color SEM image and V_g-V_{sd} conductance map for a Nb/QD/Nb device with a bottom AlOx gate, at 0 and 0.88 T. The markers indicate the correspondence between the Coulomb diamond in the two maps.

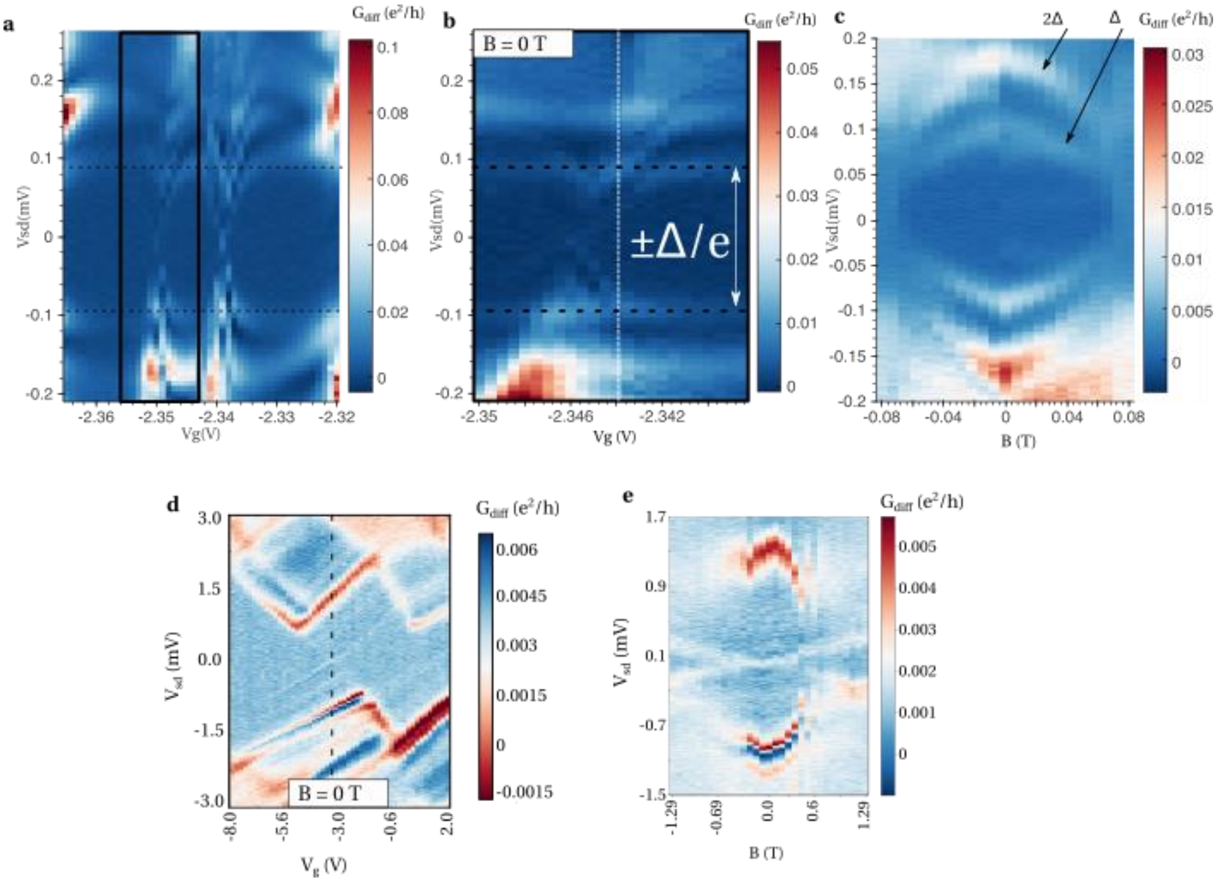

Supplementary Figure 10 | Magnetic field dependence of the control devices a and b. a, b, c. Transport characteristics of control device a: **a.** Zoom-in on the conductance map V_g-V_{sd} of the control device a (after a gate jump), at B_{ext}=0. **c.** Conductance map B_{ext} -V_{sd} at a gate voltage corresponding to the dashed line in b. **d, e.** Transport characteristics of control device b: **d.** Conductance map V_g-V_{sd} at B_{ext}=0. **e.** Conductance map B_{ext} -V_{sd} at a gate voltage corresponding to the dashed line in d. We observe the QP peak splitting and the closing of the superconducting gap reported in figure 3b.

4. Magnetic characterization of the CoPt multilayer.

In this section, we present several magnetic measures and simulations of the Co/Pt multilayered structure used in the magnetic device presented in the main text.

We present in Supplementary Fig. S11 and Supplementary Fig. S12 magnetic characterization of our CoPt multilayers. Our multilayers are characterized by SQUID magnetometry with an in- plane magnetic field, both on a plain substrate deposition (panel a) and on a chip covered of 650 nm x 30 μm stripes, processed exactly as the ones used for our bottom gates and thus expected to have the same amount of disorder (panel b). After a sharp increase for low magnetic field, the magnetization displays a slow saturation. Although the hysteresis span stays about 20 mT, the nanostructuration increases the magnetic field range for the hysteresis from 100mT to 200mT (see insets) and the saturation field from 1.5T to 2.5 T. The magnetization values at saturation differ between the two measurements due the uncertainties in the value for the volume of Co. Whatever the orientation of the applied magnetic field or the magnetic history, a low remanence is found indicating that the sample spontaneously demagnetizes. The presence of magnetic textures at zero field is doubtless in the demagnetized state, as further confirmed by magnetic force microscopy (see Fig. 1c). When approaching the saturation, the nature of the magnetic state has to be understood.

To further understand the magnetization processes in the sample, we have performed micromagnetic simulations, using the MuMax3 code[30]. As the magnetic parameters are not exactly known, the purpose is not to reproduce exactly the sample under study, but to understand qualitatively the processes, and in particular explain the field strength needed to saturate magnetization in the samples. The saturation magnetization used (1.2×10^6 A/m) has been extracted from SQUID data (panel a) and the exchange (10 pJ/m²) is the one of bulk cobalt. As the magnetic anisotropy could not be measured, we explored two hypotheses: zero effective magnetic anisotropy [exact compensation between shape ($-\frac{1}{2}\mu_0 M_s^2 = 0.905 \times 10^6 \mathrm{J}/m^3$) and interface induced anisotropies ($\frac{K_s}{\mathrm{t}} = 0.905 \times 10^6 \mathrm{J}/m^3$ with t the Co layer thickness)] and a small negative effective anisotropy ($\frac{K_s}{\mathrm{t}} = 0.7 \times 10^6 \mathrm{J}/m^3$) thus favoring in-plane magnetization orientation for homogeneous magnetized states with an effective anisotropy $K_{eff} = \frac{K_s}{\mathrm{t}} - \frac{1}{2}\mu_0 M_s^2 = -205 \times 10^6 \mathrm{J}/m^3$. These hypotheses are in agreement with litterature for the interface anisotropy at the Co/Pt interface[31]. For both cases, whatever the magnetic history is, the ground state corresponds to a demagnetized state with periodic stripes[32] (~ 100 nm period). Upon applying a magnetic field, the stripes first reorient progressively with a propagation vector orthogonal to the magnetic field to minimize the Zeeman energy in the domain walls (the domain walls being Bloch-type, their magnetization lies in the wall plane). For larger fields, the magnetization in the domains progressively rotates toward the applied magnetic field direction and saturates at about 1T. Note that textures are still observed up to the saturation. The saturation field value is to be compared to the anisotropy field $\mu_0 H_K = 2\frac{K_{eff}}{M_s}$, which is close to zero. In usual magnetic system with a low demagnetizing strength (low magnetization systems or low thickness), this would cause a saturation at field values close to

H_K. Here, the large magnetization and the ten repetitions, both favoring stripe phases, make the saturation much more difficult and therefore result in a saturation field which scales with the magnetization value. Comparing the calculated and the experimental loops we note that the saturation is much slower in the sample than in the calculation. We attribute this effect to the disorder in the sample. Indeed, due to the fabrication process the quality of the substrate could not be optimized, which results in a significant roughness. While typical roughness in good magnetic samples is about 2-5%, here larger values could be expected. We have calculated the magnetic loop with increasing roughness up to 15% thickness variation, using the roughness model successfully developed in previous studies[33,34]. While the loops are not much changed at small field, we note that due to the disorder, saturation occurs at much larger magnetic fields and the images show that magnetic textures may survive up to 2T. This validates our assumption of a smooth decrease of the synthetic spin orbit interaction used to account quantitatively for the transport data.

Additional MFM measurement under an external magnetic field were obtained, between 0 and 1.2T. Since the MFM signal is proportional to $\frac{d^2B_z}{dz^2}$, it can only give a qualitative image of the magnetic texture and as such these measures are not reproduced here. However we notice that the magnetic domains persist up to 800 mT, in rough agreement with the saturation field B_s of the observed transport oscillations (introduced below). We also noted that for the nanostructured SQUID device, the domains disappeared at lower magnetic field, illustrating the influence of disorder in our system. As a consequence, the SQUID data, even for the nanostructured device, is not perfectly representative of our device.

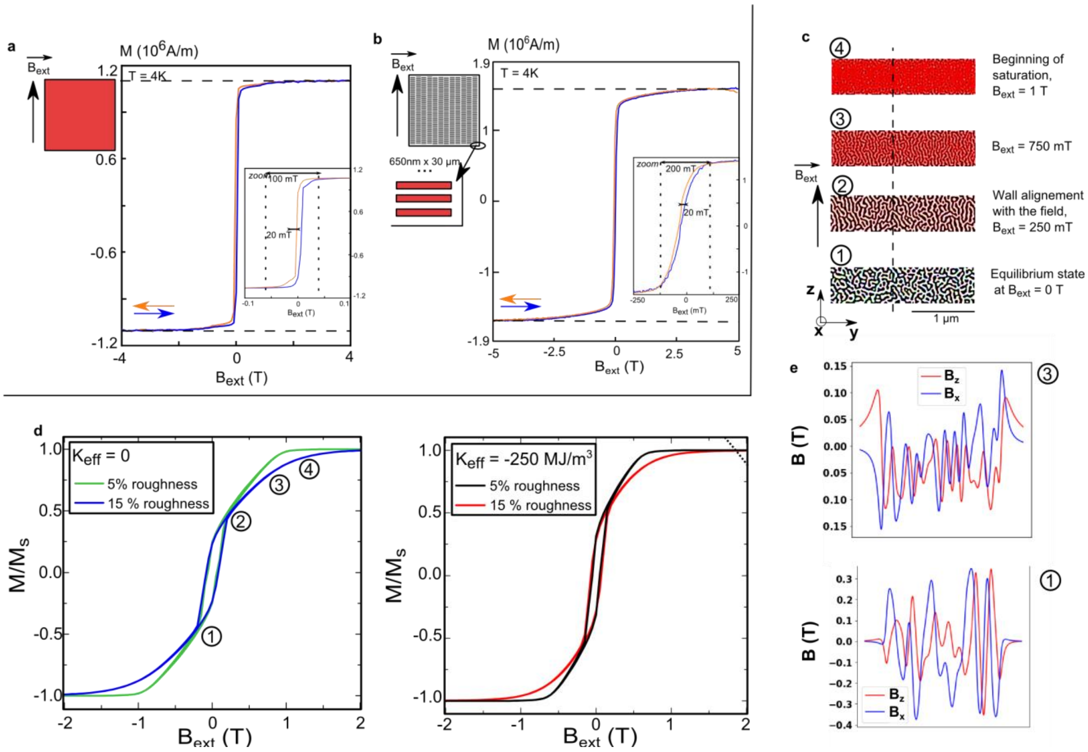

Supplementary Figure 11 | Magnetic characterization of CoPt multilayer. a. SQUID measurement at 4K of a 5mm x 5mm chip covered with the CoPt multilayer (as sketched above). The magnetization saturates at about 1.5T. Inset: Zoom on the SQUID measurement showing the opening of a hysteresis at about +/-50mT, of width 20 mT. **b.** SQUID measurement at 4K of a 5mm x 5mm chip covered with an array of the nanoscale Co/Pt stripes (such as the ones used in the transport experiment, see the layout above). The magnetization saturates only at about 2.5T. Inset: Zoom on the SQUID measurement showing the opening of a hysteresis at about +/- 100 mT, of width 20 mT. **c.** Magnetization texture for zero effective anisotropy and 15% roughness. The white and black pixels correspond respectively to up and down magnetization, the colored pixels represent the in-plane magnetization, colored according to a color wheel to represent their different orientation (red correspond to the applied field direction, see the arrow). The bottom image, numbered 1, corresponds to a virgin demagnetized state; the following are successive images from 0.25 T to 1 T (numbered 2 to 4). Images are 768 nm x 2304 nm, similar to the experimental Co/Pt gate dimensions. **d.** Calculated hysteresis loops for in-plane magnetic field, for two anisotropy hypotheses and two magnitude of roughness. **e.** Cuts of the magnetic field along the dashed line in c, obtained from the same magnetic simulation. The B_x (resp. B_z) field is represented in blue (resp. red), at a height x=10nm.

MFM characterization of another multilayered structure. We present in Supplementary Fig. S12 the AFM (height) and MFM (phase contrast) image of a trenched Co/Pt multilayered structure identical to the one of the magnetic texture device, in a more controlled environment since there was no additional processing after the deposition.

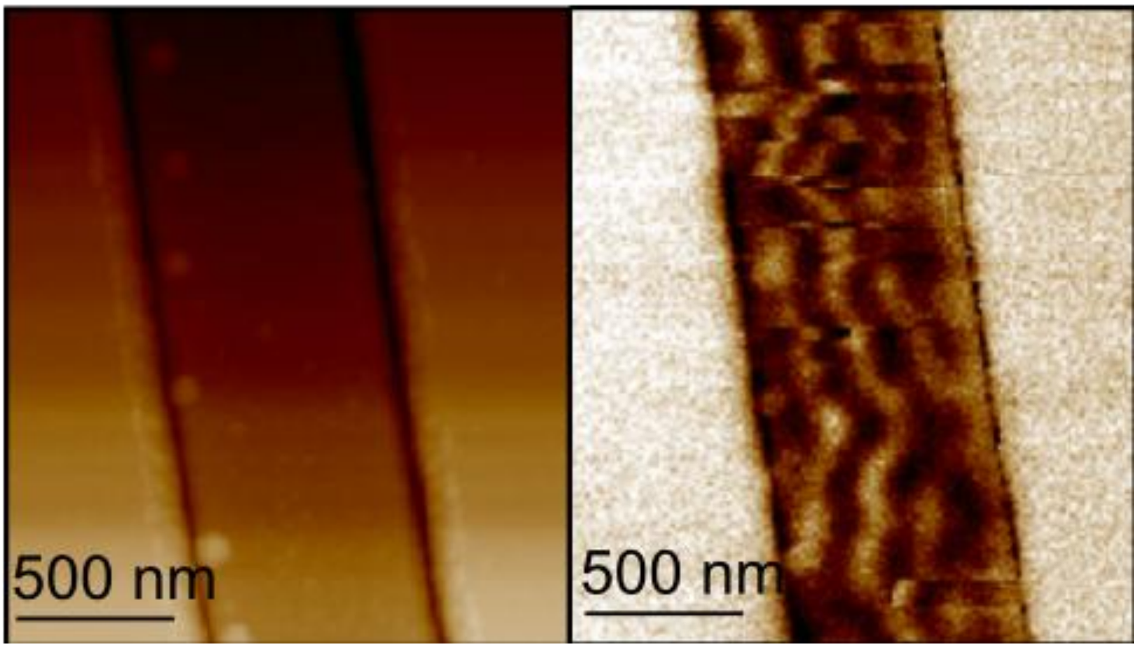

Supplementary Figure 12 | MFM image of the same Co/Pt structure in another device. Topography and phase contrast of a Co/Pt structure identical to the one of the magnetic texture device, evaporated in a trench and imaged afterwards, without any additional process as opposed to the main device. Here the MFM signal is much more regular.

5. Estimation of the synthetic spin-orbit energy from the SGSs oscillations

We here describe in more details the estimate for the spin-orbit energy from the conductance oscillations of Fig. 2.

According to the picture of Fig. 2a and b, we understand the conductance oscillations of Fig. 2 as a change in the interference condition when the number of domains $N_{dom}(B)$ changes.

The variation $E_{so}^{B_{max}} - E_{so}^{B=0}$ of the synthetic spin-orbit energy induced by $N_{dom}(B = 0) \rightarrow N_{dom}(B_{\max})$ can be related to N, the number of the SGSs oscillations by the simple formula: $E_{so}^{B_{max}} - E_{so}^{B=0} = \delta N/2$, where δ is the level spacing in the nanotube. This formula can be derived by first considering the interference condition setting the energies of the SGS, as we show below.

We model our system by a 1D conductor of length L with at one end an opaque barrier and at the other end a s-wave superconductor. The conductor has a dispersion $E(K)$ with K, the electronic wavevector.

The Andreev bound states can be derived as electronic interferences between left-moving electrons, right-moving holes, both having a wavevector K_{-}, right-moving electrons and left-moving holes, with wavevector K_{+}. The full interference process implies : one electron moving from the superconductor on the left, reflected on the opaque barrier as an electron moving back to the superconductor, reflected as a hole onto the superconductor, which is reflected again on the barrier. The interference condition is hence defined by the equation $(2K_{+}(E) - 2K_{-}(E))L = 2\pi n$. In the main text, we define $\Delta K = K_{+} - K_{-}$. This condition omits the spin degree of freedom. In absence of any polarization and spin-orbit, $K_{-} = -K_{+}$ and the two spin sectors are independent from one another. If the central conductor has a non-trivial dispersion with the spin, as is the case in figure 2a, several interferences processes can happen as shown by the orange, blue and yellow-green arrows, provided the right-mover and left-mover's spins are non-orthogonal. The latter process is the one responsible for the observed SGSs energy oscillations.

Changing the domains with the magnetic field implies that the dispersion E(K) is modified, as shown in figure 2a. The motion of the domains shifts the wave-vectors from $\Delta K^{B=0}$ to $\Delta K^{B_{max}}$. For large K, away from the helical gap, the non-orthogonal spin condition imposes that $\Delta K^{B_{max}} - \Delta K^{B=0} = 0$. Near the helical gap, the spin states are not orthogonal anymore between different branches and $\Delta K^{B_{max}} - \Delta K^{B=0} = 2k$ (yellow and green arrow), where k is the wave-vector induced by the changes in the domains.

If N oscillations of the SGS energies are detected, it means that $\Delta K^{B_{max}} - \Delta K^{B=0} = \pi N/L$, ie that k= $\pi N/2L$. For a linear dispersion, a monotonic variation of the number of domains implies that $E_{so}^{B_{max}} - E_{so}^{B=0} = \hbar v_f k = \frac{h v_f}{4LN} = \frac{\delta N}{2}$. This sets a lower bound for the synthetic orbit energy $E_{so} \gtrsim \delta \mathrm{N}/2$.

Comparing with the formula given by the unitary transformation $E_{so} = \frac{h v_F}{2\lambda} = \frac{\delta L}{\lambda}$, N oscillations of the SGSs correspond to a change in the number of domains $N_{dom} = \frac{L}{\lambda}$ of $N_{dom} = N/2$. This is in qualitative agreement with the numerical results both with the scattering and the tight-binding formalism.

6. Analytical theory of the oscillations of Subgap states with magnetic field.

We present in this section the non-interacting theory accounting for the oscillations of the subgap states as a function of the magnetic field.

The hamiltonian of the system in the normal state can be written as:

$$\widehat{H} = -\left(\frac{\hbar^2 \partial_z^2}{2m} - \mu(z)\right) + \frac{1}{2} g \mu_B \overrightarrow{B_{osc}}(z).\vec{\sigma} \qquad (1)$$

where $\vec{\sigma}$ is the spin operator of electrons and $\vec{B}(z)$ is the rotating magnetic field acting on the electron spin. The above hamiltonian can be “integrated” in order to calculate the transfer matrix $\mathcal{T}$ of a section of 1D system of length L subject to the rotating field. We note $\theta(z)$ the angle between $\overrightarrow{B_{osc}}(z)$ and the x axis as shown in Supplementary Fig.12. In the case of a regular cycloidal field which rotates at a constant speed : $\frac{\partial\theta}{\partial z} = k_{so}$, we can write the transfer matrix $\mathcal{T}$ as:

$$\mathcal{T} = exp\{i(\widehat{K} + k_{so}\hat{\mathcal{A}})L\}$$

The matrices $\widehat{K}$ and $\hat{\mathcal{A}}$ take the following expressions:

$$\widehat{K} = \begin{bmatrix} k_\uparrow & 0 & 0 & 0 \\ 0 & k_\downarrow & 0 & 0 \\ 0 & 0 & -k_\uparrow & 0 \\ 0 & 0 & 0 & -k_\downarrow \end{bmatrix} \text{and } \hat{\mathcal{A}} = \frac{1}{4\sqrt{k_\uparrow k_\downarrow}} \begin{bmatrix} 0 & k_\uparrow + k_\downarrow & 0 & k_\uparrow - k_\downarrow \\ -(k_\uparrow + k_\downarrow) & 0 & k_\uparrow - k_\downarrow & 0 \\ 0 & k_\uparrow - k_\downarrow & 0 & k_\uparrow + k_\downarrow \\ k_\uparrow - k_\downarrow & 0 & -(k_\uparrow + k_\downarrow) & 0 \end{bmatrix}$$

with $k_\sigma = \sqrt{\frac{2m}{\hbar^2}(E + \mu + \frac{1}{2}\sigma g\mu_B B_{osc})}$, μ being the chemical potential of the wire, E the energy of the electron and B_{osc} the amplitude of the oscillating magnetic field. Interestingly, the eigenmodes of the matrix $\widehat{K} + k_{so}\hat{\mathcal{A}}$ allow us to define "energy bands" even in the finite size system. We find two eigenmodes $k_\pm$ which allows us to find the two bands:

$$E_\pm(k) = -\mu + \frac{E_{SO}}{4} + \frac{\hbar^2 k^2}{2m} \pm \sqrt{\frac{\hbar^2 k^2}{2m} E_{SO} + \left(\frac{g\mu_B B_{osc}}{2}\right)^2}$$

with $E_{SO} = \frac{\hbar^2 k_{so}^2}{4m}$. This is exactly the same bands than with a Rashba spin orbit interaction with a spin-orbit wavevector $2k_{so}$ and an external magnetic field suitable for the emergence of Majorana zero modes. The corresponding energy bands and how they vary as a function of the spin orbit energy are depicted in Fig. 2 of the main text.

Note that close to the helical gap, $k_F \sim k_{so} = 2\pi/\lambda$ (ref 8 of the main text) and we recover the expression from Ref 11 of the main text, $E_{SO} = \frac{hv_F}{2\lambda}$ with λ the spatial period of the oscillations.

In order to refine the model and take into account the two end sections with homogeneous stray field as measured from the MFM, we allow two sections of lengths L_L and L_R before and after the oscillating field region with chemical potential μ_L and μ_R to be partially polarized by a magnetic field B_{pol}. The full transfer matrix of the 1D system depicted in Supplementary Fig. 12 now reads:

$$\mathcal{T}_{tot} = R(0,\mu_L,E)^{-1}R(B_{pol},\mu_L,E)exp\{i\widehat{K}_L L_L\}R\left(B_{pol},\mu_L,E\right)^{-1}R(B_{osc},\mu,E)exp\{i(\widehat{K} + k_{so}\hat{\mathcal{A}})L\}R(B_{osc},\mu,E)^{-1}R(-B_{pol},\mu_R,E)exp\{i\widehat{K}_R L_R\}R(-B_{pol},\mu_R,E)^{-1}R(0,\mu_R,E)$$

where $R(B,\mu,E)$ is the transfer matrix of each interface represented in Supplementary Fig. 12.

$$R(B,\mu,E) = \begin{bmatrix} \frac{1}{\sqrt{k_\uparrow}} & 0 & \frac{1}{\sqrt{k_\uparrow}} & 0 \\ 0 & \frac{1}{\sqrt{k_\downarrow}} & 0 & \frac{1}{\sqrt{k_\downarrow}} \\ \sqrt{k_\uparrow} & 0 & -\sqrt{k_\uparrow} & 0 \\ 0 & \sqrt{k_\downarrow} & 0 & -\sqrt{k_\downarrow} \end{bmatrix}$$

In this modeling, we assume that we have two sections around the cycloidal region in which the electrons propagate under a homogeneous magnetic field. In accordance with the magnetic simulations which shows two opposite magnetic charges at the end of the cycloidal section (due to the contribution of the inter-domains regions), we take these fields to be of the same magnitude but opposite.

The transfer matrix $\mathcal{T}_{tot}$ allows us to determine the scattering matrix $S_R(E)$ of the 1D section in the absence of superconductivity and terminated by a wall (see Supplementary Fig. 12). In the presence of a superconducting reservoir, the Subgap states energies E_{SGS} may then be found using the following identity[35] stemming from the secular equation of the system:

$$Det\{\mathbf{1} - \gamma^2 S_R(E)\hat{\sigma}_y S_R(-E)\hat{\sigma}_y\} = 0 \qquad (2)$$

where $\gamma = e^{-i\, arccos(E/\Delta)}$ is the Andreev reflection amplitude and $\hat{\sigma}_y$ is the y axis Pauli matrix.

Supplementary Fig. 13 shows a colorscale map of the Subgap states energies obtained from the secular equation (2) as a function of $\theta(L)$, the total rotation of the magnetization: N domains correspond to a total rotation of $\theta(L) = N_{dom}\pi$. We are able to reproduce the observed oscillations of the Subgap states with reasonable physical parameters using the model described above and depicted in Supplementary Fig. 13. The parameters used are the following (assuming a Landé factor of g=3.5, a similar value as the one of the control device):

$$B_{osc} = 0.47\ T, \qquad B_{pol} = 1.5\ B_{osc}, \qquad \Delta = 600\ \mu eV,$$
$$\delta = \frac{\hbar^2}{2mL^2} = 0.6\ meV\ ,\ L_L = L_R = \ L\ ,\ \mu = 0.4\ \Delta, \qquad \mu_L = \ \mu_R = 0.5\ \Delta.$$

With this model, we find that the number of oscillations of the SGSs directly corresponds to the variation in the number of domains of the magnetic texture, in agreement with the tight-binding simulations that will be presented in section 7.

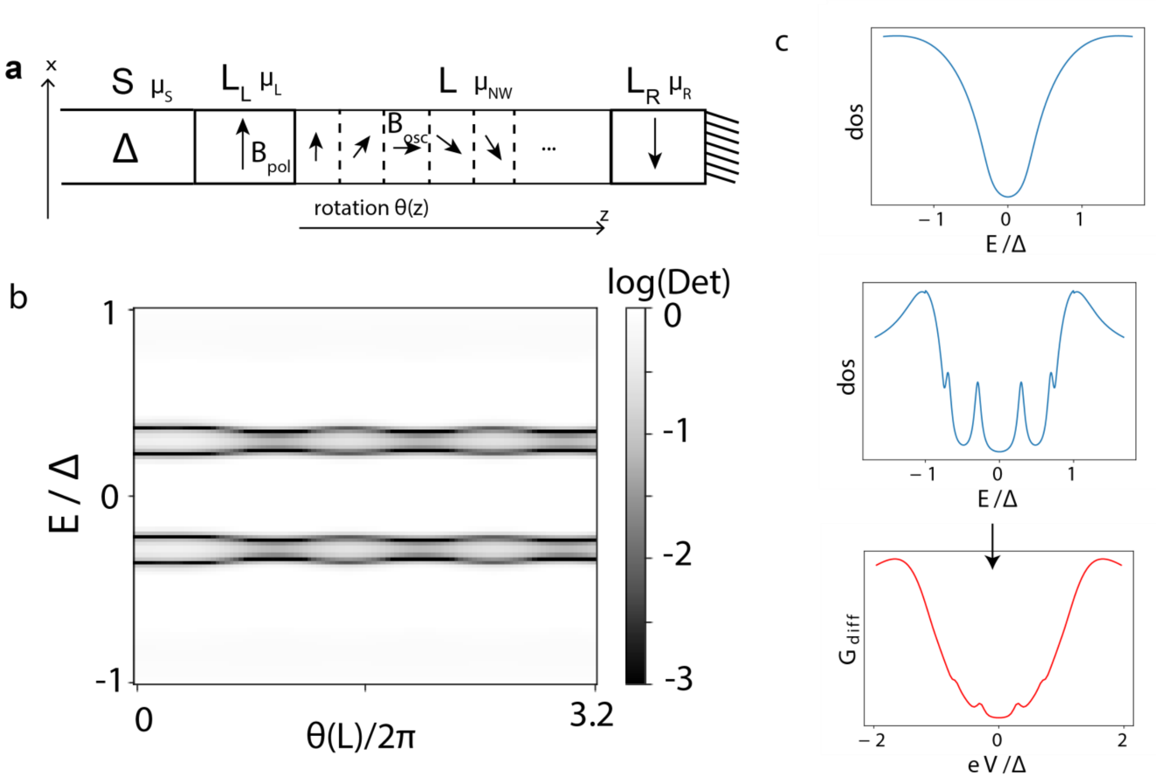

Supplementary Figure 13 | Analysis of the Subgap states oscillations. a. Schematic of the scattering representation of the device. The magnetic texture is modeled by a cycloidal field over a length L_1, and is surrounded by two short segments of length L_2 with a uniform magnetic field. It is connected to a superconductor on one side. **b.** Energy levels of the system as given by equation (2), as a function of energy and number of field oscillations, which is directly linked to the spin-orbit energy E_{so}. With parameters coherent with our experiments, we are able to reproduce several oscillations of the SGSs emergent in this device. **c.** Convolution of the density of state of a device with 2 pairs of SGSs (with energies corresponding to $0.3\ \Delta$ and $0.7\ \Delta$, a spacing that can be obtained with a slightly higher B_{osc}) and a degraded superconducting density of state (as schematized in Fig. 1). One pair of SGSs is hidden in the slope of the conductance as a function of applied bias.

Parameters used for the fit for the Fig. 3a. The oscillations in Supplementary Fig. 12 are well fitted by a simple sinusoidal function. As a consequence, we fit our oscillation data (figure 3a, grey points) with the following heuristic formula derived from the fact that they stem from interference effect and considering that the number of domains decreases linearly with the applied magnetic field (and correspondingly the spin-orbit interaction) up to a saturation value B_s:

$$eV_{sd} = \pm E_{SGS,0}(1 + a\cos[\,2\Delta k(B)L]) = \pm E_0\left(1 + a\cos\left(\frac{2\pi B}{\tilde{B}_{ext}} + \phi_0\right)\right) \text{ for } B < B_s$$

The fitting parameters are B_s= 0.9T; $\tilde{B}_{ext} = 0.56$ T; a = 0.018 meV; E_0= 0.195 meV ; ϕ_0= 0.04 where a and ϕ_0 are the amplitude and initial phase of the oscillations; it yields the purple full line in figure 3a.

We also include in the fit the closing of the superconducting gap (red line in figure 3a):

$eV_{sd} = \Delta_{\text{edge}} \sqrt{1 - \left(\frac{B}{B_c}\right)^2}$ with $\Delta_{\text{edge}} = 0.45$ meV and $B_c = 1.92$ T.

It is measured from the edge of the coherence peak due to the small bias windows of the measurement.

Large doping limit without spin orbit (Zeeman induced oscillations). In the large doping regime which allows us to linearize the dispersion relation: $k_\sigma^e \approx k_0 + \frac{E}{\hbar v_F} - \sigma \frac{g\mu_B B_{osc}}{2\hbar v_F}$ for the electrons and $k_\sigma^h \approx k_0 - \frac{E}{\hbar v_F} + \sigma \frac{g\mu_B B_{osc}}{2\hbar v_F}$, where k_0 is the Fermi wave vector. In this limiting case, equation (2) becomes, for each spin σ:

$$1 = \gamma^2 e^{2i\left(k_\sigma^e - k_\sigma^h\right)L}$$

Specifically, this equation yields the following implicit equation:

$$E_{SGS} = \pm\Delta\, cos\left\{2\pi\left(\frac{E_{SGS}}{\delta} + \sigma\frac{1}{2}\frac{g\mu_B B_{osc}}{\delta}\right)\right\}$$

In the limit of large level spacing $\delta \gg \Delta$, the above equation simply becomes:

$$E_{SGS} = \pm\Delta\, cos\left\{\pi\frac{g\mu_B B_{osc}}{\delta}\right\}$$

In case the subgap states are only subject to an external magnetic field B_{ext} (pure Zeeman effect), their evolution is obtained by making the substitution $B_{ext} = B_{osc}$. The subgap states oscillate as a function of the external magnetic field and cross at zero energy when $g\mu_B B_{ext} = \frac{\delta}{2} + n\delta, n\epsilon\mathbb{Z}$. In our case, one oscillation would require a field of 5T, an order of magnitude larger than the observed period of 600 mT.

7. Numerical study of the synthetic spin-orbit: oscillations of subgap states and emergence of Majorana zero energy modes.

In this section, we describe three studies done with the help of tight-binding simulations.

We first describe three different scenario for the evolution of SGSs as a function of an external magnetic field, which are presented in Fig. 3. Only an evolution of the magnetic domains is compatible with the oscillations observed in Fig 2.

We then study the influence of disorder in an oscillating magnetic field on conductance oscillations of SGSs. We see that the oscillations are robust to disorder, with two modeling, either relying on the MFM signal or on the magnetic simulations.

We finally investigate the emergence of MZM in our specific device geometry, where superconductivity is induced on the side. We show how two localized states at zero energy can emerge when increasing the number of oscillations of the magnetic field, as well as their evolution under local changes in the amplitude of the oscillating magnetic field.

a. Scenario of figure 3

In order to investigate numerically the evolution of subgap states with respect to different scenarii, we consider the discretized version of the hamiltonian (1) :

$$H = \sum_{n\in[1,N_1]} d_n^\dagger(-\mu\hat{\sigma}_0 + B_{osc,z}(n)\hat{\sigma}_z + B_{osc,x}(\mathrm{n})\hat{\sigma}_x + B_{osc,y}(\mathrm{n})\hat{\sigma}_y)\, d_n - t(d_n^\dagger d_{n+1} + d_n^\dagger d_{n-1})\hat{\sigma}_0 + \sum_{n\in[N_2,N_{tot}],k} t_{kn} d_n^\dagger c_k \hat{\sigma}_0 + h.c. + H_S$$

where $d_n^\dagger = \{d_{n\uparrow}^\dagger, d_{n\downarrow}^\dagger\}$ and $d_{n\sigma}^\dagger$ is the creation operator of an electron at site n and $c_k^\dagger = \{c_{k\uparrow}^\dagger, c_{k\downarrow}^\dagger\}$, the creation operator of an electron in the superconductor with momentum k, and H_S the hamiltonian of the superconductor. The chain with sites label by n is along the z-axis. The superconductor is coupled to the chain only between sites N_2 and N_{tot}. For the sake of simplicity, we take $t_{kn} = t_S$. A normal part between sites 1 and N_1 is subject to a magnetic field $B_{osc,x,y,z}(n)$. We calculate from this hamiltonian the retarded Green's function in the Nambu x Spin space at each site which allows us to obtain the conductance through the system through a Meir-Wingreen formula and the pairing function through the anomalous propagators (see for example[36]).

Supplementary Fig. 14 displays three different scenari :

A. The oscillating field is set to zero, $B_{osc}(n) = 0$ and we look at the evolution of the density of states at the first site as a function of an homogeneous field B_{ext} applied in the whole chain. The Andreev bound states display crossings at zero energy, with a period set by the energy level spacing δ. The level spacing is obtained by looking at the conductance with respect to the chemical potential μ, in the absence of the superconductor, $N_1 = N_{tot}$.

   We show a simulation for $N_{tot} = 60$, $N_1 = 30$, $N_2 = 30$, t=100, $\Delta = 1, t_s = 100, \Gamma_N = 0, \gamma_n = 0.1, \mu = 0$.

B. In scenario B, we look at the evolution of the Subgap states with respect to an external magnetic field but with a finite spin-orbit energy in the chain, modeled in the discrete Hamiltonian by an additional term : $\sum_{n\in[1,N_{tot}]} \Lambda d_n^{\dagger}\hat{\sigma}_y d_{n+1} + h.c.$ The Subgap States display anti-crossing at small magnetic field on a period which is bigger than the energy level spacing δ. We show a simulation for $N_{tot} = 60$, $N_1 = 40$, $N_2 = 20$, t=100, $\Lambda = 20$, $\Delta = 1, t_s = 1, \Gamma_N = 0, \gamma_n = 0.1, \mu = -0.99 * 2t$.

C. We then consider the scenario where the external magnetic field shifts the number of oscillations of a cycloidal field in the normal part: $B_{osc,x}(n) = B_{osc} * \cos(2\pi n\alpha)$ and $B_{osc,z}(n) = B_{osc} * \sin(2\pi n\alpha)$. We take into account the stray field out of the magnetic texture by implementing a homogeneous field in the superconducting part with amplitude 0.5 B_{osc}. The SGS show similar oscillations as observed in the experiment for which an external magnetic field is applied on the magnetic texture. We show a simulation for $N_{tot} = 60$, $N_1 = 40$, $N_2 = 20$, t = 100, $\Delta = 1, t_s = 1, \Gamma_N = 0, \gamma_n = 0.1, \mu = -0.85 * 2t, B_{osc} = 1$.

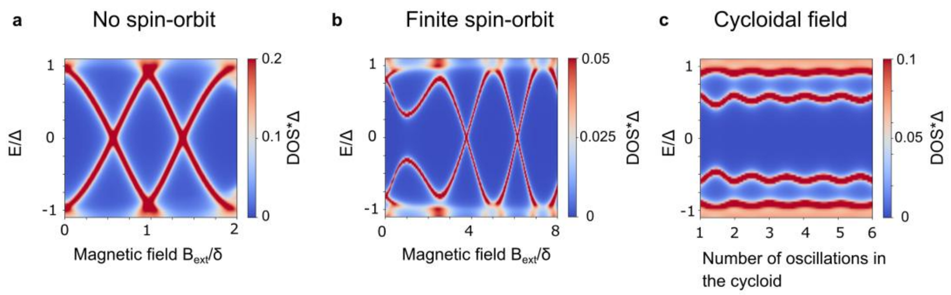

Supplementary Figure 14 | Oscillations of the Subgap states in the various situations mentioned in the table of the main text. The colorscale map displays the density of states (DOS) as a function of the energy E/Δ . Panel a (resp b) displays the evolution of Andreev Bound states as a function of a homogeneous magnetic field B_{ext} without (resp with) a spin-orbit interaction in the chain. Panel c displays the evolution of SGSs with respect to the number of oscillations of a cycloidal field in the normal part. The density of states in c shows non-crossing oscillations as a function of the number of oscillations.

b. Implementation of a realistic model for the stray fields

We now investigate the effect of disorder in the oscillating magnetic field, using the tight-binding model introduced above. We take two models for the disorder. Supplementary Fig. 15 illustrates the result of this study.

First, we consider a field that evolves in space in the same fashion as the MFM cut of Fig. 1. This signal contains various frequencies, as shown by the discrete Fourier transform given in Supplementary Fig. 7b. We construct a cycloidal magnetic field from the Fourier coefficients a_f associated with the spatial frequency f of the MFM signal in the following way:

$$B_{osc,z}(i) = B_{osc} \sum_f a_f \sin(2\pi f i)\,, B_{osc,x}(i) = \sum_f \mathrm{a_f} \cos(2\pi f i))\,.$$

We then model its evolution under an external magnetic field by a simple shift of the frequency of each coefficient of the Fourier transform. The effect of B_{ext} is:

$a_f(B_{ext}) = a_{f+\delta f(B_{ext})}$(3)

With $\delta f(B_{ext}) \propto B_{ext}$.

We use as the parameters for the discrete Hamiltonian: N_{tot} = 60, N_1 = 40, N_2 = 20, t=100, $\Delta = 1, t_s = 1, \Gamma_N = 0.2, \gamma_n = 0.15, \mu = -0.82 * 2t$. The amplitude of the oscillating field B_{osc} is normalized at each B_{ext} such that the maximal amplitude is 1 (in units of the superconducting gap □). We then plot the density of states at the first site of the chain, as a function of energy and B_{ext}. If we consider a situation where there is only one oscillation frequency, we obtain a very similar result, namely oscillations of a pair of SGSs. We conclude that disorder in the magnetic field does not strongly affect the oscillations of the SGSs predicted for a periodic magnetic field, and observed in the experiment.

As an alternative approach, we use the magnetic simulations of section 4 from which we can directly extract the magnetic field in all three directions above the Co/Pt structure, and its evolution as a function of the external magnetic field. This is shown in Supplementary Fig. 15f. We use as the parameters for the discrete Hamiltonian: N_{tot} = 60, N_1 = 40, N_2 = 20, t=100, $\Delta = 1, t_s = 1, \Gamma_N = 0, \gamma_n = 0.15, \mu = -0.85 * 2t$. The amplitude of the oscillating field is taken as:

B_{osc} (units of Δ) $= 2\ B_{magnetic\ simulations}$(T)

in order to have a qualitative agreement with the measured oscillations, for this set of parameters.

The micro-magnetic simulations give the spatial evolution of the field vector B_{osc} for seven values of B_{ext} : 0, 0.2, 0.4, 0.6, 0.8, 1 and 1.2T. We interpolate linearly the evolution of each component of the field in between these seven values. We plot the density of states at the first site as a function of energy and B_{ext}, and observe oscillations of the SGSs energies, under this more realistic evolution of the magnetic texture. The simulations reproduce qualitatively the evolution of B_{osc} in the three direction of space, at different elevations above the texture, when a magnetic field is applied to the magnetic texture. At different cut positions we can obtain different realizations for B_{osc}. The simulated fields used for this study may not perfectly fit our sample's stray field; notably it seems to contain more domains than what the MFM signal indicates.

To conclude, this show that the analysis of the oscillations of the SGSs is robust considering more realistic models of our system, build either from a realistic stray field profile extracted from the MFM data, or from micro-magnetic simulations.

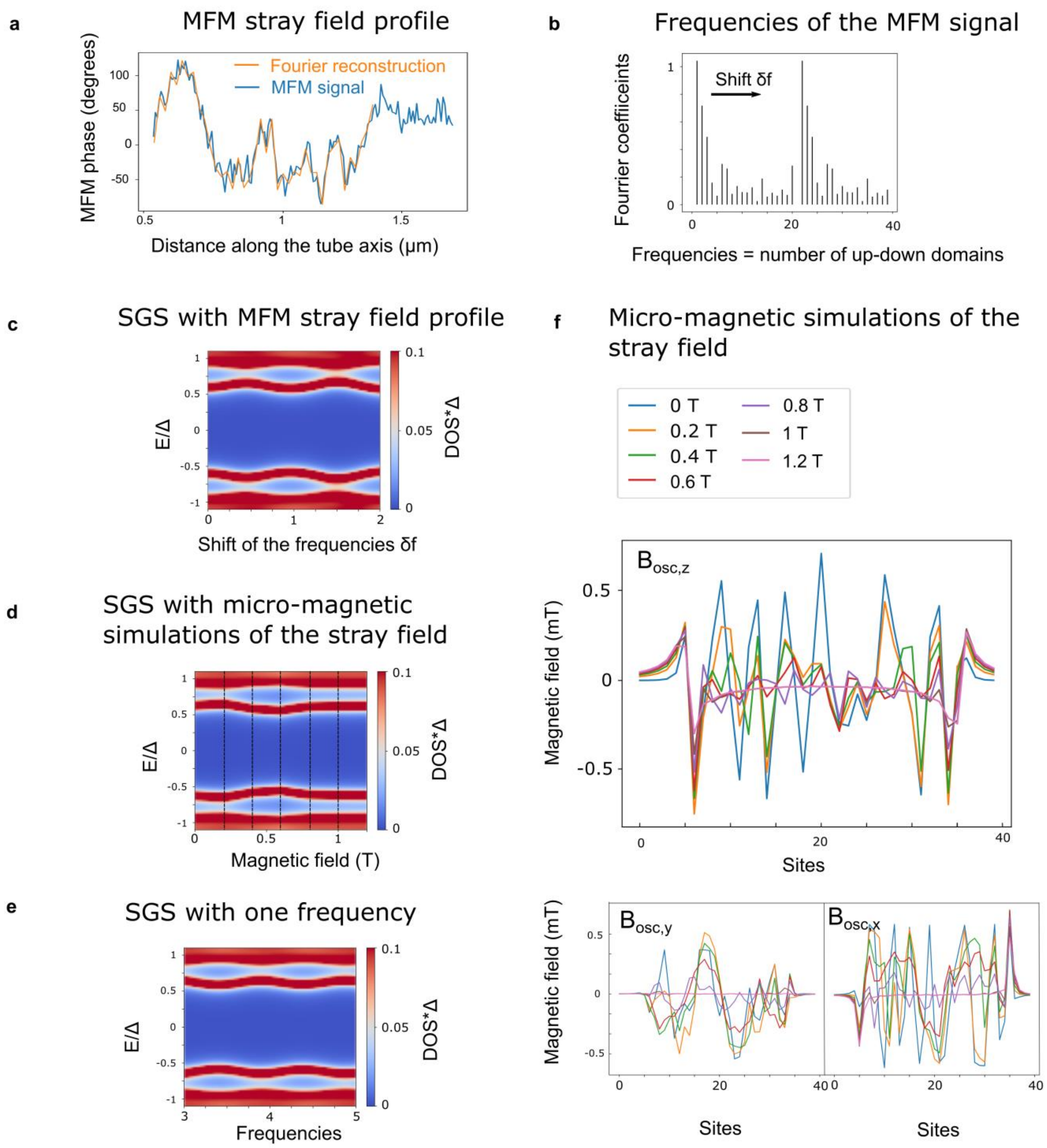

Supplementary Figure 15 | Effect of disorder in the oscillating magnetic field. a. Cut of the MFM image along the CNT as represented in Fig. 1 of the Main Text (in blue), and reconstructed signal containing the N=40 top-most frequencies of the discrete Fourier transform of the raw data (orange). **b.** Modulus of the Fourier coefficients of the MFM signal of a. A given discrete frequency can be thought of as the number of up and down domains in the magnetic texture. To mimic the effect of the external magnetic field, we shift the coefficients' frequency as shown in equation (3). For example, the coefficient corresponding to 5 oscillations at the beginning will, at $\delta f = 2$, correspond to 7 oscillations. **c.** Density of states of a one-dimensional wire as a function of the energy showing Subgap States (SGSs). The oscillating field is given by the orange curve of panel a and evolves under a shift of it Fourier coefficients. The x axis corresponds to shifting frequencies. **d.** The oscillating magnetic field is now taken from the magnetic simulations, in all three directions of space. **e.** Similar plot, with only one coefficient in the discrete Fourier transform. **f.** Oscillating magnetic field in all three directions of space, extracted from the magnetic simulations, along the dashed line in Supplementary Fig. 7d. It is given for different external magnetic fields, at a height x=0nm.

c. Simulation of Majorana bound states in our geometry

We now turn to the situation where Majorana zero modes can potentially emerge in our setup. Our setup is different from the ones which are a priori used in semiconducting systems. We show in Supplementary Fig. 16 the relevant figures. We study the variations of the density of states (DOS), the singlet pairing and the triplet pairing as a function of the number of magnetic domains (which are tuned by the external magnetic field in the experiment). The parameters of the model are given below

$N_{tot} = 20$, $N_1 = 16$, $N_2 = 15$, t=12, $\Delta = 1, t_s = 12, \Gamma_N = 0.1, \gamma_n = 0.05, \mu = -0.33 * 2t, B_{osc} = 8$.

The density of states shown in Supplementary Fig. 16a displays oscillations of Subgap states at non zero energy but more importantly a zero bias peak emerging when the number of domains increases. In order to characterize the Subgap states, it is instructive to plot the singlet and triplet pairing amplitudes (in panel b and c) for the same parameters. Interestingly, before the emergence of the zero bias peak, one sees both singlet and triplet pairing amplitudes as expected for superconductivity in the presence of homogeneous spin polarization. However, the emerging zero bias peak is solely made out of triplet correlations, as required for a Majorana zero mode. The singlet pairing amplitude is defined as $\frac{\left|G^R\left(d_\uparrow^\dagger,d_\downarrow^\dagger\right)-G^R\left(d_\downarrow^\dagger,d_\uparrow^\dagger\right)\right|}{\sqrt{2}}$, where G is the retarded Green's function, and e (resp. h) refers to electrons (resp. holes). The triplet pairing amplitude is defined as $\sqrt{\frac{1}{2}\left|G^R\left(d_\uparrow^\dagger,d_\downarrow^\dagger\right)+G^R\left(d_\downarrow^\dagger,d_\uparrow^\dagger\right)\right|^2+\left|G^R\left(d_\uparrow^\dagger,d_\uparrow^\dagger\right)\right|^2+\left|G^R\left(d_\downarrow^\dagger,d_\downarrow^\dagger\right)\right|^2}$.

We now show another important feature of this zero mode: its spatial localization and sensitivity to the local configuration of the magnetic field, as illustrated in panels e, f and g. These colormaps show the density of state as a function of the position in the chain and energy, for a system with the same parameters as panel a and with 7 magnetic field oscillations (14 domains). As expected, we see that the zero bias peak corresponds to two localized states located at the interface between the magnetic texture and the superconductor and the magnetic texture and the left hard wall. On the contrary, the non-zero energy Subgap States are fully delocalized on the entire wire length. Importantly a change in the magnetic texture has barely any effect on the later irrespectively of the position of this change (Supplementary Fig. 16h and i). This is completely different from the case of the Majorana zero mode which is insensitive to a local reconfiguration of the magnetic texture if this reconfiguration occurs in the middle of the wire (Supplementary Fig. S16h) whereas it splits, with a decrease of the ZBP conductance, if the reconfiguration occurs close to the superconducting/wire interface where its wave function is non-zero (Supplementary Fig. S16i). The localized states at zero bias have a larger weight for the spin triplet amplitude than for the spin singlet amplitude as shown in panels e and f of figure S16.

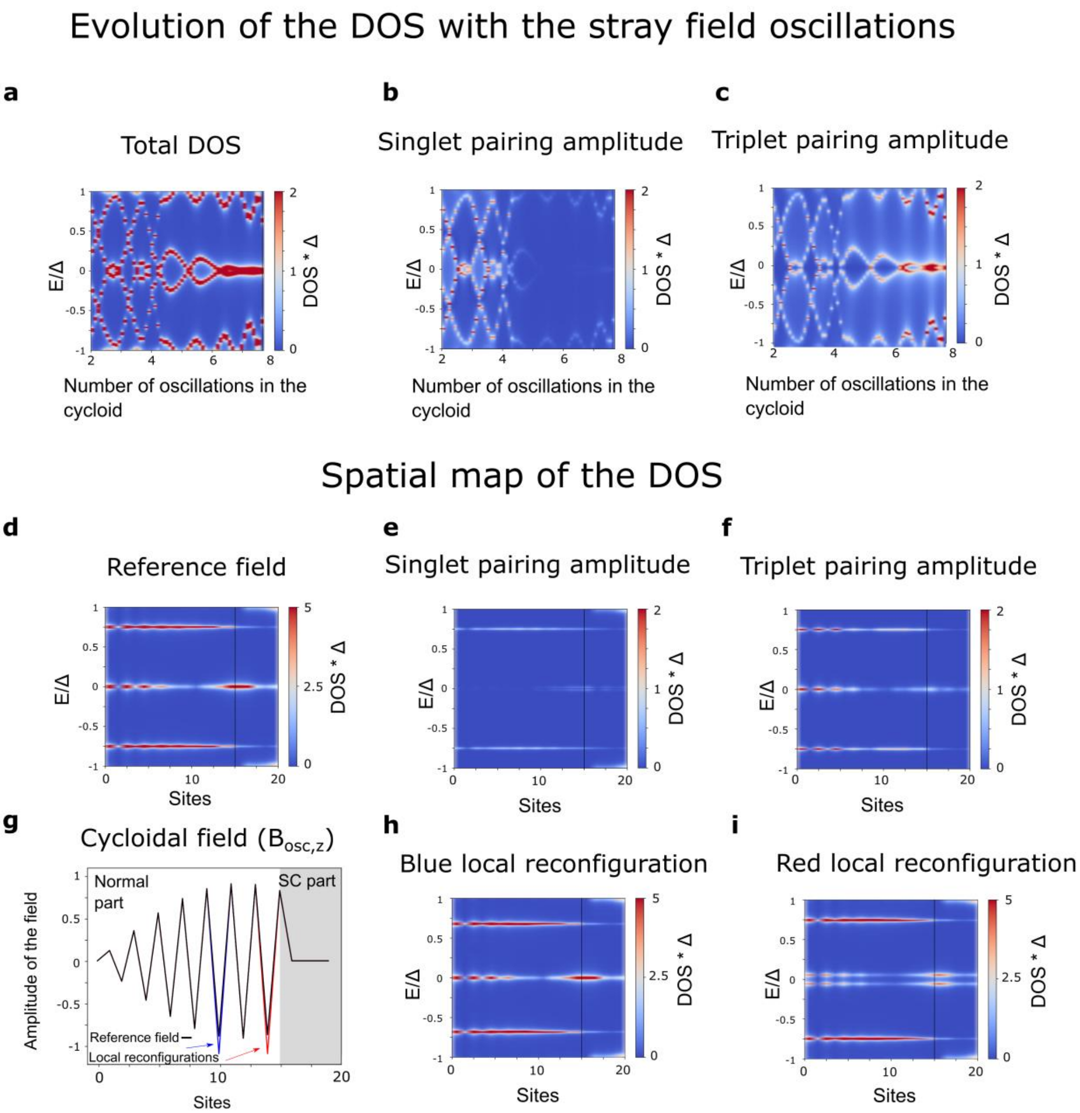

Supplementary Figure 16 | Emergence of Majorana excitations in our experimental setup. a. Density of states (DOS) at the first site of the chain (site 0), computed using a discretized tight-binding Hamiltonian, showing the emergence of a zero-bias peak for a large number of up and down domains. **b-c.** shows the singlet and triplet pairing amplitude for the same parameters. Singlet and triplet pairing amplitude are defined in the text of this supplementary. **d**. The spatial dependence of the DOS shows two localized states at zero biais, with a larger weight for the spin triplet amplitude (colormap **f**) than for the spin singlet amplitude (colormap **e**). The numerical simulation is realized by considering a normal part with a cycloidal field, as illustrated in g for the component along the axis of the chain (z-axis), plotted in black and labelled reference field. The field is not perfectly sinusoidal because of the high ratio between the number of oscillations (7) and the number of sites (16) for the cycloid. A superconductor is connected to the chain from sites 15 to 20. Two scenarii for a local reconfiguration of the field are shown in red and blue. **d, h** and **i** display the spatial dependence of the density of states for the three different configurations of the field (black, red and blue). The dotted line shows the separation between the normal part and the superconducting part.

All these features reproduce qualitatively our experimental findings and show that localized Majorana zero modes can emerge when superconductivity is induced from the side of the wire, in a different manner than the initial proposals for engineering Majorana bound states in a one dimensional conductor.

In summary, our numerical study confirms the robustness to disorder of the oscillations of the SGSs at non-zero energy and substantiate the Majorana zero mode interpretation of the observed zero bias peak.

30. Vansteenkiste, A. *et al.* The design and verification of mumax3, *AIP Advances*, **4**, 107133 (2014).

31. Beauvillain, P. *et al.* Magnetic interface anisotropy in ultrathin cobalt films Au/Co/M/Au, with M = Au, Cu, Pd or Pt, *J. Magn. Magn. Mat,.* **121**, 503 (1993)

32. Tekielak, M. et al. The effect of magnetostatic coupling on spin configurations in ultrathin multilayers, *J. Appl. Phys.*, **107**, 083911 (2010).

33. Jue, E. *et al.* Domain wall dynamics in ultrathin Pt/Co/AlOx microstrips under large combined magnetic fields, *Phys. Rev. B*, **93,** 014403 (2016).

34. Pham, T. H. *et al.* Very large domain wall velocities in Pt/Co/GdOx and Pt/Co/Gd trilayers with Dzyaloshinskii-Moriya interaction, *Europhys. Lett.,* **113**, 67001 (2016).

35. C.W.J. Beenakker, Lect. Notes Phys. **667**, 131 (2005).

36. Bruhat, L. E. *et al*., Cavity Photons as a Probe for Charge Relaxation Resistance and Photon Emission in a Quantum Dot Coupled to Normal and Superconducting Continua. *Phys. Rev. X* **6**, 021014 (2016).